

## Maximal Air Bubble Entrainment at Liquid-Drop Impact

Wilco Bouwhuis, Roeland C. A. van der Veen, Tuan Tran, Diederik L. Keij, Koen G. Winkels, Ivo R. Peters, Devaraj van der Meer, Chao Sun, Jacco H. Snoeijer, and Detlef Lohse

*Physics of Fluids Group, Faculty of Science and Technology, MESA+ Institute, and Burgers Center for Fluid Dynamics, University of Twente, 7500AE Enschede, The Netherlands*

(Received 21 May 2012; revised manuscript received 10 July 2012; published 26 December 2012)

At impact of a liquid drop on a solid surface, an air bubble can be entrapped. Here, we show that two competing effects minimize the (relative) size of this entrained air bubble: for large drop impact velocity and large droplets, the inertia of the liquid flattens the entrained bubble, whereas for small impact velocity and small droplets, capillary forces minimize the entrained bubble. However, we demonstrate experimentally, theoretically, and numerically that in between there is an optimum, leading to maximal air bubble entrainment. For a 1.8 mm diameter ethanol droplet, this optimum is achieved at an impact velocity of 0.25 m/s. Our results have a strong bearing on various applications in printing technology, microelectronics, immersion lithography, diagnostics, or agriculture.

DOI: [10.1103/PhysRevLett.109.264501](https://doi.org/10.1103/PhysRevLett.109.264501)

PACS numbers: 47.55.D–

The impact of liquid droplets on surfaces is omnipresent in nature and technology, ranging from falling raindrops to applications in agriculture and inkjet printing. The crucial question often is: How well does the liquid wet a surface? The traditional view is that it is the surface tension which gives a quantitative answer. However, it has been shown recently that an air bubble can be entrapped under a liquid drop as it impacts on the surface [1–6]. Also, Xu *et al.* [7,8] revealed the important role of the surrounding air on the impact dynamics, including a possible splash formation. The mechanism works as follows [3–6]: The air between the falling drop and the surface is strongly squeezed, leading to a pressure buildup in the air under the drop. The enhanced pressure results in a dimple formation in the droplet and eventually, to the entrapment of an air bubble [Fig. 1(a)]. The very simple question we ask and answer in this Letter is: For which impact velocity is the entrapped bubble maximal?

Our experimental setup is shown in Fig. 1(b) and is similar to that of Refs. [9,10] where it is described in detail. An ethanol drop impacts on a smooth glass surface after detaching from a needle, or for velocities smaller than 0.32 m/s, after moving the needle downwards using a linear translation stage. A high-speed side view recording is used to measure the drop diameter and velocity. The experiment is carried out at room temperature. A synchronized bottom view recording by a high-speed color camera is used to measure the deformed shape of the liquid drop. Colored interference patterns are created by high-intensity coaxial white light, which reflects from both the glass surface and the bottom of the droplet. Using a color-matching approach in combination with known reference surfaces, the complete air thickness profile can be extracted [shown in Fig. 1(c)]. For experiments done at larger impact velocities ( $U > 0.76$  m/s), we use a pulse of diffused laser light triggered by an optical switch. The thickness of the air

film at the rim is assumed to be zero, and the complete air thickness profile can then be obtained from the monochromatic fringe pattern. From these measurements, we can determine the dimple height,  $H_d$ , and the volume of the entrained bubble,  $V_b$ , at the very moment of impact. This moment is defined by the first wetting of the surface. This is the moment when the concentric symmetry of the interference rings is lost, since due to unavoidable tiny tilts of the glass plate the wetting, in general, is nonaxisymmetric. To calculate the bubble volume  $V_b$ , we integrate the thickness profile of the air layer trapped beneath the drop. Note that the dimple profiles and the volume of the entrained bubble are obtained *before* the wetting occurs, such that we do not have to take into account the properties of the surface (e.g., contact angle or roughness, which is of the order of 10 nm). Alternatively, we can also measure the volume of the trapped bubble after impact when the liquid already wets the surface. Both measurements provide the same results. In the present Letter, we use the first approach.

The results are shown in Fig. 2. Clearly, both dimple height at impact and the size of the entrained bubble have a pronounced maximum as function of the impact velocity  $U$ . The corresponding impact velocity for which the air entrainment is optimal is  $U_o = 0.25$  m/s for an ethanol droplet of radius  $R = 0.9$  mm (or the Stokes number  $St_o = 1 \times 10^4$ ). While length scales are given in multiples of the droplet radius  $R$ , following Brenner and coworkers [3,6], we express the impact velocity  $U$  in terms of the Stokes number  $St$ , defined with the dynamic air viscosity  $\eta_g = 1.82 \times 10^{-5}$  Pa s and the liquid density  $\rho_l$  as  $St = \rho_l R U / \eta_g = \rho_l / \rho_g Re$ , where  $Re = \rho_g R U / \eta_g$  is the standard Reynolds number. A further relevant parameter of the system is the surface tension  $\gamma$ , which can be expressed in terms of the Weber number  $We = \rho_l R U^2 / \gamma$  or in terms of the capillary number  $Ca = \eta_g U / \gamma = We / St$ .

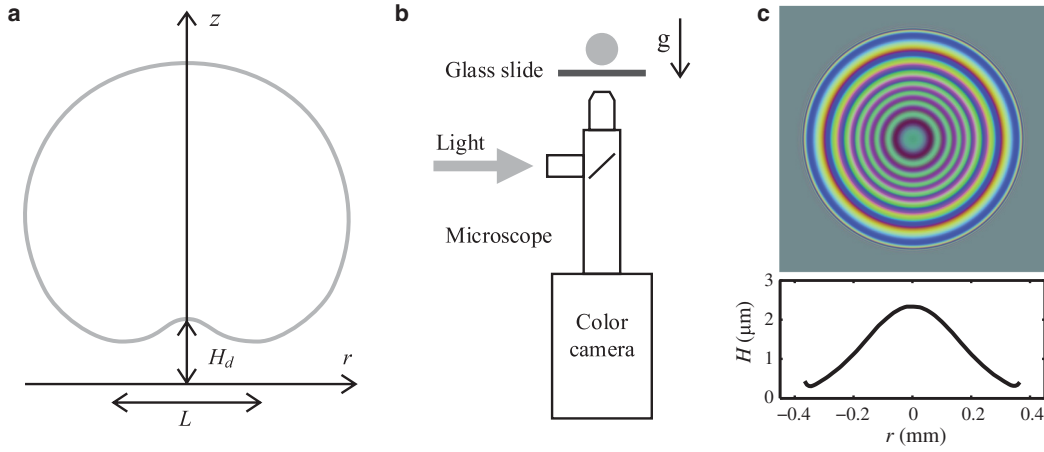


FIG. 1 (color). Experimental characterization of air bubble entrapment. (a) Sketch of dimple formation (not drawn to scale) just prior to impact. (b) Schematic of the experimental setup used to study droplet impact on smooth surfaces. An ethanol droplet of typical radius  $R = 0.9$  mm falls on a glass slide of average roughness 10 nm. The impact velocity is varied by varying the falling height of the droplet. For very small velocities below 0.31 m/s, the droplet is fixed at the tip of 0.4 mm—diameter capillary that is vertically translated downwards at a constant velocity. The bottom view is captured by a high-speed color camera (SA2, Photron Inc.). The camera is connected to a long working-distance microscope and a  $5\times$  objective to obtain a 2 mm field of view. (c) An example of an interference pattern and the extracted air thickness profile. Note the difference in horizontal and vertical length scales. The exposure time was  $1/15\,000$  s and the typical frame rate of the recordings is 5000 frames per second.

We compare and supplement our experimental findings on the dimple height at impact and the entrained bubble size to numerical results. The numerics consists of an axisymmetric boundary integral (BI) simulation for the liquid droplet (i.e., the droplet is assumed to obey potential flow), coupled to a lubrication approximation of the Stokes equation

$$\frac{\partial P_g}{\partial r} \sim \eta_g \frac{\partial^2 u_r}{\partial z^2}, \quad (1)$$

that describes the viscous, incompressible gas flow under the droplet [3,11–14]. Here,  $z$  is the vertical direction,

$P_g(r, t)$  is the gas pressure, while  $u_r$  is the radially outward velocity in the gas parallel to the surface [Fig. 1(a)]. Note that the gas flow under the droplet is indeed viscous: An upper bound for the Reynolds number relevant for the lubrication flow gives  $UH_d/\nu_g \sim 0.1$  for the highest impact velocity, and is typically much smaller for most of our experiments.

We now give more details on the numerical simulation: The velocity field inside the droplet is described with a scalar velocity potential  $\phi$ , obeying the Laplace equation  $\nabla^2 \phi = 0$ . The axisymmetric droplet contour is described using cylindrical coordinates  $r, z$  and is solved numerically

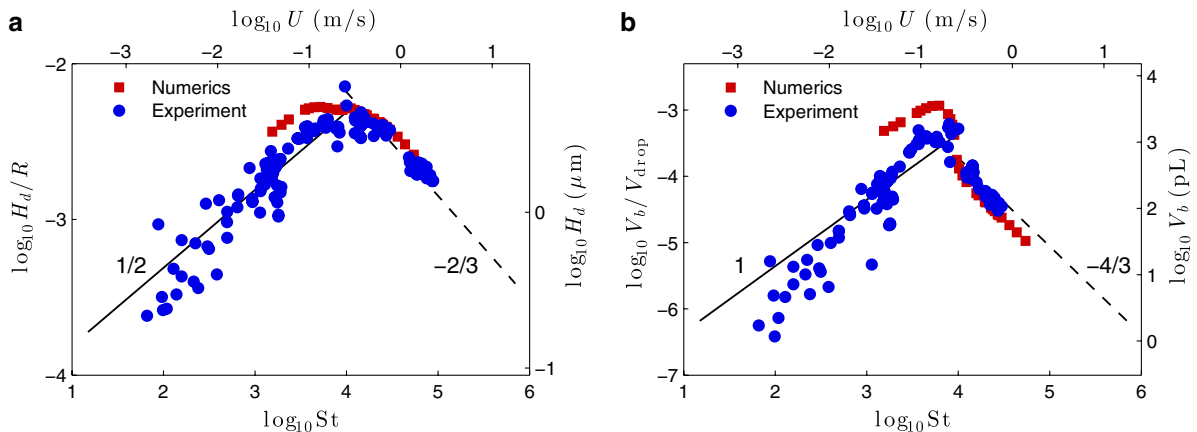


FIG. 2 (color online). Maximum entrapment of air bubbles. (a) Dimple height  $H_d$  and (b) entrained bubble volume  $V_b$  as functions of the impact velocity  $U$  (upper axes) and Stokes number  $St$  (lower axes). The shape of the air layer can be characterized by the dimple height  $H_d$  and the lateral extension  $L$ . Blue circles correspond to high-speed color interferometry measurements, red squares correspond to numerical simulations. The straight lines correspond to the derived scaling laws in the capillary regime (solid) and inertial regime (dashed) with the respective scaling exponents.

by using the BI method; the simulations are based on the numerical code described in Refs. [15–17]. This BI simulation is an alternative way of solving the system of equations, compared to the method applied in Ref. [11], in which case a Hilbert transform method was applied. In contrast to Ref. [14], we do not solve the complete Navier–Stokes equations, but do include dynamics of the air layer below the drop. The dynamic boundary condition on the droplet contours is given by the unsteady Bernoulli equation,

$$\left(\frac{\partial \phi}{\partial t} + \frac{1}{2} |\nabla \phi|^2\right) = -gz - \frac{\gamma}{\rho_l} \kappa(r, t) - \frac{P_g(r, t) - P_\infty}{\rho_l}. \quad (2)$$

Here,  $t$  is time,  $g$  the acceleration of gravity,  $z$  the absolute height,  $\kappa(r, t)$  the interface curvature, and  $P_\infty$  the far-field pressure. The key dynamical quantities in Eq. (2) are the gas pressure  $P_g(r, t)$  and the interface curvature  $\kappa(r, t)$ . The curvature is related to the dimple profile  $H(r, t)$  by the geometric relation

$$\kappa(r, t) = \frac{\frac{\partial^2 H(r, t)}{\partial r^2}}{\left[1 + \left(\frac{\partial H(r, t)}{\partial r}\right)^2\right]^{3/2}} + \frac{\frac{\partial H(r, t)}{\partial r}}{r \left[1 + \left(\frac{\partial H(r, t)}{\partial r}\right)^2\right]^{1/2}}. \quad (3)$$

To close the problem, an additional equation is provided by the lubrication approximation for the viscous gas flow at the bottom of the droplet,

$$\frac{\partial H(r, t)}{\partial t} - \frac{1}{r} \frac{\partial}{\partial r} \left[ \frac{r(H(r, t))^3}{12\eta_g} \frac{\partial P_g(r, t)}{\partial r} \right] = 0, \quad (4)$$

with boundary condition  $P_g|_{r=R} = P_\infty$ ; the gas pressure at the top of the droplet is set to atmospheric. Contrarily to Ref. [11], we do not incorporate effects of compressibility of the gas, since, following the analysis of Ref. [13], there is little influence of compressibility in the regime that is studied here. The initial conditions for the simulations consist of a spherical droplet with radius  $R$  with a downward velocity  $U$ . The initial height is taken sufficiently high for the pressure induced by the radial velocity profile to be still negligible as compared to the ambient pressure ( $\sim 10 \mu\text{m}$ ). The number of nodes on the droplet surface for which the BI equations are solved is of order 100, with node density increasing for  $r \rightarrow 0$ . The number of nodes and the size of the time steps vary during the simulation, as a function of the local gap height and velocity of the droplet contour. The size of a time step is of order 10 ns. For any number of nodes, the coupling between gap height and pressure profile breaks down for some small value of  $H$ , since the pressure diverges at vanishing thickness of the air layer. Consistent with the experimental resolution, we continue our simulations until the minimum gap thickness reaches  $0.4 \mu\text{m}$ , while ensuring that our algorithm remains accurate. This is the moment at which the values for  $H_d$  and  $V_b$  are extracted, which, however, have already achieved their final value much earlier, as shown in the Supplemental Material [18].

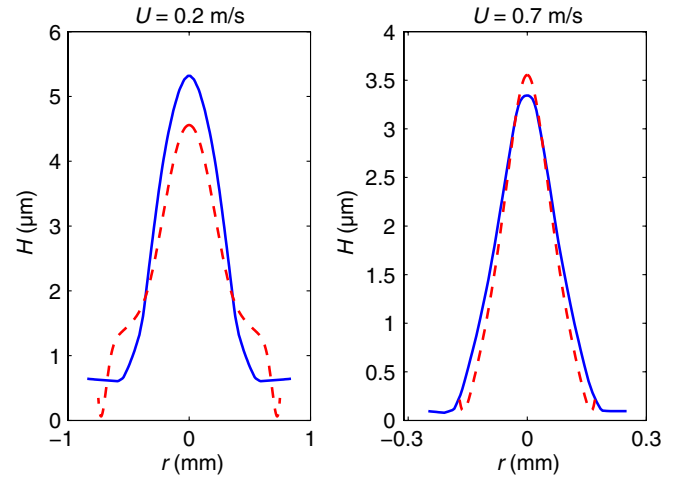


FIG. 3 (color online). Comparison of experimental (blue, solid) and numerical (red, dashed) dimple profiles for two different impact velocities;  $U = 0.2 \text{ m/s}$  ( $St = 7.8 \cdot 10^3$ ; crossover regime) and  $U = 0.7 \text{ m/s}$  ( $St = 2.7 \cdot 10^4$ ; inertial regime).

The results of the numerical calculations are shown in Fig. 2, together with the experimental data, showing very good agreement with our experimental results: in particular, we observe the pronounced maxima in the dimple size and in the entrained bubble volume at the optimal Stokes number  $St_c$ . In the numerically obtained bubble volume, we observe a jump exactly at the crossover regime. This jump originates from a change in the shape of the dimple. Figure 3 compares the experimental and numerical dimple profiles for an impact velocity at the crossover regime ( $U = 0.2 \text{ m/s}$ ) and an impact velocity in the inertial regime ( $U = 0.7 \text{ m/s}$ ). While the profiles are in excellent agreement in the inertial regime (both volume and dimple height), the numerical profile develops a “double dimple” at the lower impact speed. This variation in shape results in the jump observed for the numerical bubble volumes in the crossover regime [see Fig. 2(b)]. In all cases, however, the dimple height  $H_d$  is in quantitative agreement without any adjustable parameters.

Numerical and experimental results together suggest a scaling  $H_d/R \sim St^{-2/3}$  for larger Stokes numbers, while  $H_d/R \sim St^{1/2}$  for smaller Stokes numbers. We will now theoretically derive these scaling laws. For large  $St$ , we follow and extend Refs. [6,12,19]: The horizontal length scale  $L$  of the dimple extension [see Fig. 1(a)] follows from geometrical arguments as  $L \sim \sqrt{H_d R}$ , and  $u_r$  from mass conservation as  $u_r \sim UL/H_d$ . The Stokes Eq. (1) suggests  $P_g \sim L\eta_g u_r/H_d^2$  as an estimate for the gas pressure below the falling drop at touch-down. The liquid pressure  $P_l$  can be estimated from the unsteady Bernoulli equation: dimensional analysis gives the deceleration time scale  $H_d/U$  and the potential in the liquid  $\sim UL$ , resulting in  $P_l \sim \rho_l U^2 L/H_d$ . Since the liquid drop will be deformed when  $P_g \sim P_l$ , one finally obtains the scaling for the dimple height and the bubble volume:

$$H_d \sim RSt^{-2/3}, \quad V_b \sim L^2 H_d \sim R^3 St^{-4/3}. \quad (5)$$

This describes the air bubble in the inertial regime, i.e., large impact velocities, in agreement with our experimental and numerical findings.

For small  $St$ , corresponding to small impact velocity and small droplet radius, capillarity will take over and tries to smoothen the dimple out. Then the pressure inside the gas must be balanced with the Laplace pressure  $\gamma\kappa$ . Under the assumption that the horizontal length again scales as  $L \sim \sqrt{H_d R}$ , the dimple curvature  $\kappa \sim H_d/L^2$ . Using once more that the gas pressure  $P_g \sim L\eta_g u_r/H_d^2$ , one immediately obtains

$$\frac{H_d}{R} \sim \sqrt{Ca} \sim \sqrt{We/St} \sim \frac{\eta_g}{\sqrt{\gamma\rho_l R}} St^{1/2},$$

$$\frac{V_b}{R^3} \sim \frac{\eta_g^2}{\gamma\rho_l R} St, \quad (6)$$

as scaling in the capillary regime. Again, this agrees well with the experimental and numerical findings. The cross-over between the regimes, determined by the maximum dimple height, occurs at

$$St_o \sim Ca_o^{-3/4} \quad \text{or} \quad U_o \sim \frac{\eta_g^{1/7} \gamma^{3/7}}{\rho_l^{4/7} R^{4/7}}. \quad (7)$$

Using prefactors obtained from our experimental data in Fig. 2, for an ethanol droplet of 0.9 mm radius, this translates to an impact velocity  $U_o = 0.25$  m/s. What is the physical reason for the maximum? For higher velocities, inertia dominates and flattens the droplet at impact. For lower velocities and/or smaller droplets, the capillary forces try to keep the drop spherical. In between these two regimes, the maximal air entrainment under the droplet is achieved.

For many applications, air entrainment is undesirable and maximal wetting must be achieved. This holds for immersion lithography, wafer drying, glueing, and agricultural applications [20,21]. Intriguingly, for inkjet drops of radius  $R \sim 10 \mu\text{m}$ , the optimal velocity according to Eq. (7) is approximately 1 m/s. This lies exactly in the range at which inkjet usually operates (typically a few m/s), and relatively large bubbles will, thus, be entrapped [1]. For immersion lithography, the entrapment of even micron-sized bubbles can cause practical limitations [20,21]. This technology is based on optical imaging of nanoscale structures, for which the optics is immersed in water to push the limits of spatial resolution. Clearly, it is crucial to avoid bubbles or to minimize their size, which also has bearing in

cleaning and drying of wafers. Ideally, one should stay as far as possible from the optimal air entrainment impact velocity. Our findings will help to achieve this goal and thus, optimal wetting.

We gratefully acknowledge helpful discussions with Christophe Clanet. This study was financially supported by NWO, FOM, an ERC advanced grant, and ASML.

- 
- [1] D. van Dam and C. L. Clerc, *Phys. Fluids* **16**, 3403 (2004).
  - [2] S. Thoroddsen, T. Etoh, K. Takehara, N. Ootsuka, and A. Hatsuki, *J. Fluid Mech.* **545**, 203 (2005).
  - [3] S. Mandre, M. Mani, and M. P. Brenner, *Phys. Rev. Lett.* **102**, 134502 (2009).
  - [4] M. M. Driscoll and S. R. Nagel, *Phys. Rev. Lett.* **107**, 154502 (2011).
  - [5] J. M. Kolinski, S. M. Rubinstein, S. Mandre, M. P. Brenner, D. A. Weitz, and L. Mahadevan, *Phys. Rev. Lett.* **108**, 074503 (2012).
  - [6] S. Mandre and M. P. Brenner, *J. Fluid Mech.* **690**, 148 (2012).
  - [7] L. Xu, W. W. Zhang, and S. R. Nagel, *Phys. Rev. Lett.* **94**, 184505 (2005).
  - [8] L. Xu, L. Barcos, and S. R. Nagel, *Phys. Rev. E* **76**, 066311 (2007).
  - [9] R. C. A. van der Veen, T. Tran, D. Lohse, and C. Sun, *Phys. Rev. E* **85**, 026315 (2012).
  - [10] M. H. W. Hendrix, R. Manica, E. Klaseboer, D. Y. C. Chan, and C.-D. Ohl, *Phys. Rev. Lett.* **108**, 247803 (2012).
  - [11] M. Mani, S. Mandre, and M. P. Brenner, *J. Fluid Mech.* **647**, 163 (2010).
  - [12] P. D. Hicks and R. Purvis, *J. Fluid Mech.* **649**, 135 (2010).
  - [13] P. D. Hicks and R. Purvis, *Phys. Fluids* **23**, 062104 (2011).
  - [14] J. Eggers, M. A. Fontelos, C. Josserand, and S. Zaleski, *Phys. Fluids* **22**, 062101 (2010).
  - [15] H. N. Oguz and A. Prosperetti, *J. Fluid Mech.* **257**, 111 (1993).
  - [16] R. P. H. M. Bergmann, D. van der Meer, S. Gekle, J. van der Bos, and D. Lohse, *J. Fluid Mech.* **633**, 381 (2009).
  - [17] S. Gekle and J. M. Gordillo, *Int. J. Numer. Methods Fluids* **67**, 1456 (2011).
  - [18] See Supplemental Material at <http://link.aps.org/supplemental/10.1103/PhysRevLett.109.264501> for technical details of the experiments and simulations.
  - [19] F. T. Smith, L. Li, and G. X. Wu, *J. Fluid Mech.* **482**, 291 (2003).
  - [20] M. Switkes, M. Rothschild, T. A. Shedd, H. B. Burnett, and M. S. Yeung, *J. Vac. Sci. Technol. B* **23**, 2409 (2005).
  - [21] K. G. Winkels, I. R. Peters, F. Evangelista, M. Riepen, A. Daerr, L. Limat, and J. H. Snoeijer, *Eur. Phys. J. Special Topics* **192**, 195 (2011).